

# OptiGAN for Crystal Arrays: Physics-Informed Generative Modeling of Optical Photon Transport in PET Detector Arrays

Stephan Naunheim<sup>1</sup> , Brandon Pardi<sup>2</sup> , Guneet Mummaneni<sup>2</sup> , Carlotta Trigila<sup>1</sup>, Emilie Roncali<sup>1</sup> 

<sup>1</sup>Department of Biomedical Engineering, University of California, Davis, Davis, CA, United States of America

<sup>2</sup>Department of Computer Science, University of California, Davis, Davis, CA, United States of America

E-mail: [snaunheim@ucdavis.edu](mailto:snaunheim@ucdavis.edu)

## Abstract.

*Objective.* Monte Carlo simulations of optical photon transport are computationally prohibitive for large-scale optical systems including detector arrays and PET systems, restricting their practical use to single-crystal studies. This work presents an enhanced conditional generative adversarial network (optiGAN) capable of replacing optical simulations at the crystal array level, extending our previous single-crystal approach to a  $3 \times 3$  BGO detector array.

*Approach.* We enhance the Wasserstein-GAN framework with Fourier feature encoding, a learnable latent mapping network, and a physics-informed loss term enforcing momentum conservation. Training data requirements are reduced eight-fold by exploiting the array's symmetry. The model evaluation employs three complementary studies. First, a full array evaluation testing whether training on the fundamental domain generalizes to the complete detector geometry, second, a high-resolution study probing out-of-distribution generalization to emission positions not seen during training, and third, a pencil beam  $\gamma$ -photon irradiation study assessing practical applicability under conditions relevant to experimental detector characterization. The performance is benchmarked against GATE10/Geant4 ground truth data, using the intrinsic statistical fluctuations between independent Monte Carlo runs as baseline.

*Main results.* The enhanced optiGAN achieves sliced Wasserstein similarity values within  $3\sigma$ -agreement of the Monte Carlo baseline across all evaluation conditions, demonstrating successful generalization from the fundamental training domain to the full crystal array and robust interpolation to untrained emission positions. Notably, the model successfully transitions from electron-emission training data to realistic  $\gamma$ -photon interactions, producing flood maps that accurately reproduce characteristic experimental patterns including photopeak clusters and inter-crystal scatter lines.

*Significance.* This proof-of-concept demonstrates that physics-informed generative models can accurately simulate optical photon transport in segmented scintillator arrays while maintaining computational accessibility. The successful reproduction of experimentally relevant flood map features, including photopeak clusters and inter-crystal scatter lines, validates optiGAN as a practical tool for PET detector development. This work establishes a foundation for future models capable of generalizing across diverse array configurations.

*Keywords:* PET, GAN, simulation, physics-informed

## 1. Introduction

Positron emission tomography (PET) is a medical imaging technique [1–3] that aims to provide functional information on physiological processes within a subject. Imaging relies on the registration of coincident annihilation quanta using dedicated radiation detectors, which often consist of scintillation crystals coupled to readout sensors [4]. Although PET research is multifaceted, one major branch focuses on advances in detection instrumentation to improve the information available for image reconstruction. Typically, Monte Carlo simulations [5–7] are used to evaluate the feasibility of, for example, novel detector concepts or data-processing algorithms. Although these simulations represent the gold standard, the time required to run them is often long due to stepwise particle tracking and, therefore, prohibitive for large-scale detector system setups.

Furthermore, one is often not interested in every detail of individual particle tracks (e.g., reflections, transmission, binary scattering flag), but rather in the signals produced by the sensor that can be used in experiments. One approach to reduce simulation time is to use generative models [8–15] that directly produce information at the readout sensor level and do not rely on tracking particles through the detection medium. This new approach potentially offers new insights into detector modeling by allowing the user to generate only signals and data that satisfy specified conditions, which might be challenging to achieve in classical Monte Carlo simulations constrained by physical laws. However generative models must be trained to learn the relevant statistical distributions, which requires time and the availability of training data that provide *de facto* ground truth. For this reason, the primary application of generative AI modeling will likely be at the detector and system levels rather than at the level of single crystals.

In previous research [15–17], our group demonstrated the feasibility of building a conditional generative adversarial network (GAN) [18–20], called optiGAN, that can replace optical simulations at the single crystal level. Furthermore, we integrated the model into the open-source GATE10 ecosystem, enabling interested users to test and work with it.

In this new proof-of-concept study, we present a novel model in the optiGAN family designed to operate on crystal arrays rather than single crystals. Although the current implementation, including training overhead, does not outperform conventional optical simulations in total computation time yet, this work provides essential insights into array-level generative modeling that will guide future training efficiency optimizations. The GAN can be used to generate data representing the detection of optical photons at the attached sensor surfaces based on the conditioned location of the  $\gamma$ -photon interaction in the crystals. The generation includes the spatial coordinates ( $\mathbf{R}_i = (x_i, y_i)^T$ ) of an impinging optical photon  $i$ , its energy ( $E_i$ ), and the time of detection ( $T_i$ ). In addition, the model generates the normalized directional momentum components ( $\hat{\mathbf{P}}_i = (p_{x,i}, p_{y,i}, p_{z,i})^T$ ), which are not directly relevant in experimental settings but provide a means to introduce physics-informed knowledge into the model. Compared with our previously published OptiGAN model, we introduce three significant architectural changes to account for the increased complexity of modeling crystal arrays rather than single crystals while maintaining computational accessibility for typical GATE users. First, we augment the latent vector with Fourier components [21, 22] with the aim of helping the model learn non-smooth, step-wise distributions, which are expected to be seen at the boundaries between neighboring crystals. However, while this approach greatly enriches the latent representation, it also drastically increases the dimensionality of the latent space, which is a non-desired side effect for our use case. Therefore, we employ a small learnable mapping network [23] as a preprocessor for the generator input, selecting and weighting the important components of the augmented latent vector to compress the input to the generator's original dimensionality. Following this strategy, we can build more complex models without a significant increase in computational cost relative to our previously published single-crystal model. The last significant modification addresses the adversarial loss function by adding a physics-informed loss term that softly enforces momentum conservation for the optical photons.

We apply the optiGAN model to simulated data of a Bismuth Germanate (BGO) array consisting of  $3 \times 3$  crystals, each with a volume of  $3 \text{ mm} \times 3 \text{ mm} \times 10 \text{ mm}$ . The model is trained on data from only one eighth of the array's quadratic base area (fundamental domain). Still, we test its capabilities with distinct studies

using the full-crystal array, a high-resolution study, and a practical use case with pencil-beam irradiation.

## 2. Materials & Methods

### 2.1. Physics-informed OptiGAN with Latent Fourier Augmentation

We extend the classical OptiGAN architecture [15–17], which follows a Wasserstein-GAN [20] design with gradient penalty [24], with three key innovations to improve sample quality and enforce physical constraints (see Figure 1) for properly modeling the crystal array. The innovations include changes in the latent space and loss function, such that the core network architecture of the generator and discriminator, which worked for single crystals, remains unchanged. Each modification introduces a new set of hyperparameters. Given the proof-of-concept nature of this study, we did not perform an extensive hyperparameter optimization. Instead, a small set of commonly used hyperparameter values was evaluated to validate the core idea.

*Fourier Feature Encoding* To address the spectral bias of neural networks, which struggle to learn high-frequency functions, we augment the input latent vector  $\mathbf{z} \in \mathbb{R}^d$  with Fourier feature encoding [22],

$$\gamma(\mathbf{z}) = [\sin(2^k \pi \mathbf{z}), \cos(2^k \pi \mathbf{z})]_{k=0}^{n_{\text{freq}}-1} \in \mathbb{R}^{2nd}, \quad (1)$$

where  $n_{\text{freq}}$  controls the number of frequency components. This transformation provides the network with explicit multi-scale representations, enabling it to capture fine-grained details and sharp features that are difficult to learn from raw noise alone.

In this work, we follow our prior publications and use  $d = 7$  original latent features. The number of Fourier frequencies is set to  $n_{\text{freq}} = 4$ , based on the results of a preliminary limited hyperparameter search.

*Latent Mapping Network* Rather than directly passing the high-dimensional noise vector to the generator, which heavily increases computational load, we employ a learnable latent mapping network [23] that adaptively combines the original latent vector and its Fourier encoding,

$$\mathbf{z}^* = f_{\text{mapper}}([\mathbf{z}, \gamma(\mathbf{z})]; \theta_m), \quad (2)$$

where  $f_{\text{mapper}}$  is a two-layer MLP with LeakyReLU activation that maps the concatenated  $d + 2nd$  dimensional input back to  $d$  dimensions. This network learns to weight and combine frequency components optimally for the generation task, reducing dimensionality while preserving important spectral information.

*Physics-Informed Loss* Depending on the emission location of the optical photons, the attached sensors capture different distributions of photon momenta due to geometric constraints, e.g., reflections. Those distributions carry physical meaning, since they show allowed and forbidden regions in the momentum space, which becomes especially important at crystal boundaries where transmission and reflection occur. To softly enforce physical constraints on generated samples, we incorporate conservation of the optical photons' momenta  $\hat{\mathbf{P}}_i$  in the loss function. For photon momenta  $\hat{\mathbf{P}}_i$  in a batch  $\mathcal{I}$ , the physics loss  $\mathcal{L}_{\text{phy}}$  is defined as

$$\mathcal{L}_{\text{phy}} = \mathbb{E} \left[ \left( \sum_{i \in \mathcal{I}} \hat{\mathbf{P}}_i^T \hat{\mathbf{P}}_i - 1 + \varepsilon \right)^2 \right] + \beta \cdot \text{Var} \left( \sum_{i \in \mathcal{I}} \hat{\mathbf{P}}_i^T \hat{\mathbf{P}}_i \right) \quad (3)$$

where  $\varepsilon$  and  $\beta$  are hyperparameters controlling the softness and relative weighting of the constraint. The variance term encourages tight adherence to the constraint across all samples. This loss is combined with the adversarial WGAN-GP objective  $\mathcal{L}_{\text{adv}}$  using an annealing schedule  $\lambda(t)$ ,

$$\mathcal{L}_{\text{gen}} = \mathcal{L}_{\text{adv}} + \lambda(t) \cdot \mathcal{L}_{\text{phy}}, \quad (4)$$

that linearly increases from 0 to the target weight over a warmup period, allowing the generator to first learn the overall data distribution before enforcing physical constraints. In this proof-of-concept study, we use a strict constraint ( $\varepsilon = 0$ ) of momentum conservation, while the variance term is not penalized

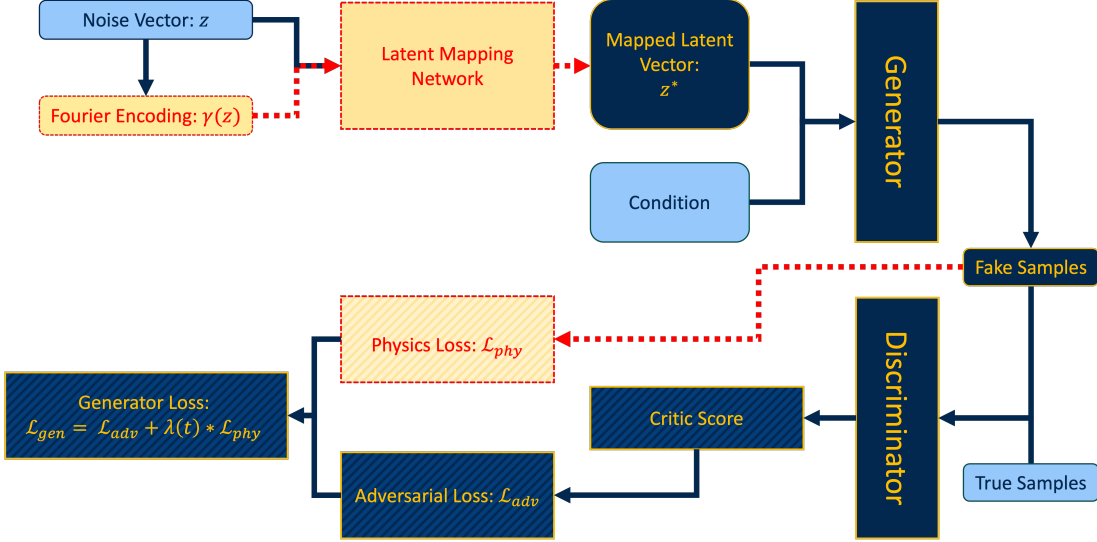


Figure 1: Schematic architecture of the enhanced optiGAN model. Rectangles in yellow represent newly introduced modifications for properly modeling the crystal array. Input data is marked as light blue rectangles. The generator and discriminator design have not been changed.

$(\beta = 0)$ . We chose a warmup period of 5000 epochs, with a target weight of  $\lambda(t \geq 5000) = 0.01$ . The complete generator architecture processes the mapped latent representation  $\mathbf{z}^*$ , concatenated with the condition labels  $\mathbf{y}$ , through a four-layer MLP with ReLU activations to produce the final output. The discriminator follows a similar architecture with dropout regularization ( $p = 0.1$ ) to prevent overfitting.

### 2.2. PET Detector & General Simulation Settings

The simulated PET detector (see Figure 2) is comprised of  $3 \times 3$  BGO crystals. Each crystal has a base area of  $3\text{ mm} \times 3\text{ mm}$  and a height of 10 mm. Each crystal is coupled to an silicon photomultiplier (SiPM), modeled as a  $200\text{ }\mu\text{m}$  thick  $\text{SiO}_2$  layer. The optical coupling between the crystal and SiPM is given as an Epoxy layer with a thickness of  $200\text{ }\mu\text{m}$ . All crystals have polished surfaces and are optically separated from one another using Teflon (diffuse reflection). Optical surfaces are modeled using the Davis LUT model [25–27].

Simulations are conducted with GATE10 [6, 7] using the `G4EmStandardPhysics_option4` physics list. The production cuts within the crystals are set to  $10\text{ }\mu\text{m}$ . Phasespace actors attached to the crystals and sensor volumes are used to cluster optical photon data from the same initial interaction event.

### 2.3. Fundamental-Domain Training Dataset

The crystal array's square geometry induces a  $D_4$  point group symmetry. This symmetry manifests as invariance under  $90^\circ$  rotations and mirror reflections, which translates to the absence of preferential light propagation directions. By exploiting this symmetry, it is possible to limit the training data creation to the so-called fundamental domain  $\mathcal{F}$  of the array's base area,

$$\mathcal{F} = \{(x, y) : 0 \leq y \leq x \leq L/2\}, \quad (5)$$

with  $L$  denoting the side length of the array. Any point outside this region can be mapped to it through an appropriate symmetry operation  $g \in D_4$  to a point in the fundamental domain. Since  $\mathcal{F}$  covers only about an eighth of the full array area, this technique allows an eight-fold reduction in computational time and memory requirement.

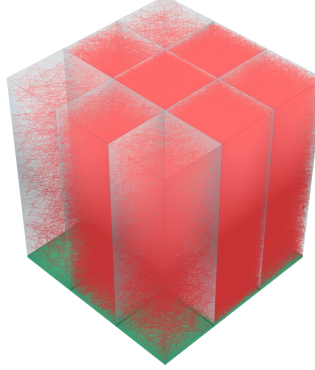


Figure 2: Simulated crystal array consisting of  $3 \times 3$  BGO crystals.

The isotropic emission of mono-energetic electrons ( $E_{e^-} = 420$  keV) at specific locations within the crystals is simulated to create training and testing data. The emission locations are distributed on a regular grid with a step size of 0.6 mm over the fundamental domain and define the conditions fed into the GAN. The grid is repeated at a height of 1 mm, 5 mm, and 9 mm from the sensor surface to include multiple depth-of-interactions (DOIs). Approximately  $3 \times 10^4$  optical photons are recorded for each emission location and included in the training dataset, which is equivalent to the sum of optical photons one would see considering the geometric efficiency for a total of  $\sim 25$  photoelectric absorptions of 511 keV-annihilation quanta.

### 3. Methodology

#### 3.1. Distributional Similarity

To quantitatively evaluate the quality of generated samples, we employ the sliced Wasserstein distance (SWD), which efficiently approximates the high-dimensional Wasserstein distance via random one-dimensional projections. This metric captures differences in the full multivariate distribution structure while remaining computationally tractable, and provides stable gradients even for non-overlapping distributions.

To obtain a normalized similarity metric in  $[0, 1]$ , we compute a baseline distance between the real data distribution and a Dirac delta distribution centered at zero ( $D_{\text{baseline}} = \text{SWD}(\mathbf{p}_{\text{real}}, \delta_0)$ ). The normalized sliced Wasserstein similarity (SWS) is then defined as

$$\text{SWS} = 1 - \frac{\text{SWD}(\mathbf{p}_{\text{real}}, \mathbf{q}_{\text{gen}})}{D_{\text{baseline}}}, \quad (6)$$

where a value of 1 indicates a perfect distributional match. This normalization makes the metric interpretable and invariant to feature scale.

In our implementation, we use  $K = 60$  random projections and subsample both distributions to 50,000 points. Rather than evaluating performance globally, we compute the SWS for each condition separately to assess the generator's accuracy across different spatial regions within the crystal array, enabling identification of regions where the generator performs well or requires improvement.

#### 3.2. Visual Similarity

From an instrumentalist perspective, the detailed distributional analysis presented in Section 3.1 addresses quantities that are often difficult to access experimentally. Momentum distributions, for instance, are not measured in typical PET systems, and the optical photon signals themselves undergo multi-step transformations, including applying the SiPM response, which inhibits photon detection efficiency, dark

counts, and electronic noise before reaching the data acquisition system. Consequently, for practical applications, it is more meaningful to evaluate the agreement using metrics that reflect standard experimental characterization procedures employed in instrumentation research. Therefore, we compare GAN-generated and Monte Carlo floodmaps using the structural similarity index measure (SSIM) [28]. Unlike pixel-wise metrics, the SSIM accounts for the perceptual quality of image structures and is particularly sensitive to the preservation of shapes, edges, and spatial patterns. In the context of flood maps, this translates to detecting whether the GAN correctly reproduces characteristic clustering patterns, e.g., photopeak and inter-crystal scatter events, practically determining detector performance. For two image patches  $\mathbf{x}$  and  $\mathbf{y}$  (local regions of the flood map), the local SSIM is defined as

$$\text{SSIM}(\mathbf{x}, \mathbf{y}) = \frac{(2\mu_x\mu_y + C_1)(2\sigma_{xy} + C_2)}{(\mu_x^2 + \mu_y^2 + C_1)(\sigma_x^2 + \sigma_y^2 + C_2)}, \quad (7)$$

where  $\mu_x$  and  $\mu_y$  are the local means,  $\sigma_x^2$  and  $\sigma_y^2$  are the local variances,  $\sigma_{xy}$  is the local covariance, and  $C_1, C_2$  are constants to stabilize the division. The global SSIM (in the following manuscript referred to as SSIM) is computed over sliding windows, based on an uneven number of pixels, across the entire flood map and averaged to produce a global similarity score ranging from  $-1$  (no similarity) to  $+1$  (perfect similarity).

For this evaluation, image resolution plays a crucial role, and in the context of SiPMs, a meaningful resolution is the typical size of single photon avalanche diode (SPAD). State-of-the-art SiPMs for PET have SPAD [29] sizes that can range from  $10\text{ }\mu\text{m}$  to  $100\text{ }\mu\text{m}$ . We therefore utilize an effective floodmap resolution of  $50\text{ }\mu\text{m}$  by using a sliding window of  $5 \times 5$  pixels combined with a histogram binning of  $10\text{ }\mu\text{m}$ .

*Bootstrap Confidence Intervals* Providing uncertainty estimates for visual similarity poses two challenges that prevent the adoption of the approach used in Section 3.1. First, the  $\gamma$ -photon interaction positions along the  $Z$ -axis are distributed continuously throughout the crystal volume, rather than lying on a regular grid, as in the electron-emission experiments. This precludes the condition-by-condition analysis employed for the SWS metric, in which the variance across discrete grid points provides a natural measure of uncertainty. Second, the flood map is an image with strongly non-uniform count statistics (high-count photopeak clusters at crystal centers and lower-count inter-crystal scatter lines).

To obtain statistically well-founded uncertainty estimates under these conditions, we employ bootstrap resampling. For each comparison, we generate  $N_{\text{bootstrap}} = 100$  resampled datasets by randomly drawing (with replacement) from the original center-of-gravity (COG) coordinate distributions. For each iteration, we recompute the flood map histograms and evaluate the SSIM.

### 3.3. Evaluation Experiments

The model's generation capabilities are evaluated using three distinct studies. In each experiment, the model's performance is compared with the ground truth from state-of-the-art GATE10 simulations. To account for the natural fluctuations of Monte Carlo simulations, each evaluation dataset is simulated twice under the exact same simulation settings. Subsequently, the evaluation metrics are applied to compare the two runs and determine the maximum similarity achievable by the GAN.

*Full Array Evaluation* In a first study, the model is evaluated on the full crystal array domain. In this step, we test how the model performs under conditions outside the fundamental domain while maintaining the exact spatial sampling as for the training dataset. The complete dataset incorporates three different DOI-layers (1 mm, 5 mm, 9 mm), like the training dataset, while each layer holds 225 electron emission locations covering the full crystal array. At each source location 30 monoenergetic electrons ( $E_{e^-} = 420\text{ keV}$ ) are emitted. The baseline is provided by the condition-averaged SWS value from two Monte Carlo simulations, along with its standard deviation. This baseline is justified because Monte Carlo simulations rely on the same physical models and interaction cross-sections across all conditions, ensuring uniform accuracy regardless of the specific emission location. This assumption cannot be made a priori for the GAN model,

as its learned representation may exhibit spatially varying fidelity across different emission conditions. We therefore adopt a more detailed evaluation approach: The SWS is computed individually for each emission point, and we subsequently analyze whether the resulting means and standard deviations are consistent across rows and columns of the emission grid for a given DOI-layer. This allows us to identify potential systematic biases in the model's performance as a function of spatial position within the crystal array.

*High-Resolution Evaluation* A fundamental distinction between Monte-Carlo simulations and learned generative models lies in their spatial generalization behavior. Monte Carlo methods, grounded in first-principles physics, produce accurate results for any emission location within the defined geometry. In contrast, generative models learn distributions from discrete training conditions, raising the question of whether they can reliably interpolate to emission locations not explicitly represented during training. To investigate this potential limitation, we use a high-resolution dataset probing the model's out-of-distribution generalization capabilities. While training data is acquired on a coarse spatial grid of 0.6 mm step width at a distance from the sensor face of 1 mm, 5 mm, and 9 mm (see Section 2.3), the high-resolution dataset uses a much finer step width of 0.25 mm at 1 mm, 3 mm, 5 mm, 7 mm, and 9 mm height. At each source location 30 monoenergetic electrons ( $E_{e^-} = 420$  keV) are emitted. This experimental design enables systematic assessment of whether the model has learned a continuous, physically meaningful mapping from emission coordinates to optical photon distributions, or whether its performance degrades for conditions lying between training positions. Such interpolation capability is essential for practical applications where arbitrary interaction locations must be modeled accurately.

Because high-resolution sampling significantly increases the number of emission locations and, consequently, the simulation time and storage requirements, we limit ourselves to emission locations within the fundamental domain. Furthermore, sources located exactly at the crystal boundaries ( $\{(x, y) : x = 1.5 \text{ mm} \vee y = 1.5 \text{ mm}\}$ ) are excluded from the evaluation dataset, as the physical behavior at these interfaces is mathematically ill-defined for both the Monte-Carlo Simulation as well as the GAN.

Following the evaluation methodology established in the full array study, we compute the SWS individually for each emission condition and analyze spatial consistency across the grid, considering the row and column mean values and standard deviations. For conditions that are located in a row or column having fewer than four other conditions, the row or column-averaged standard deviation is used.

*Pencil Beam Evaluation* While electron emission within the crystal array provides a well-controlled setting for generating high-fidelity training and evaluation datasets, a more realistic scenario arises when annihilation photons are created outside the detection volume and impinge on the array's surface. Besides that, often in experimental PET detector characterization, the primary quantity of interest is not the detailed optical photon distribution itself, but rather the resulting flood map typically computed via COG estimation from the sensor signals. In practice, floodmaps are the standard tool for assessing crystal identification and separation quality in pixelated scintillator arrays, as they distinguish between photopeak and inter-crystal scatter events.

To evaluate the model's performance in this practical use case, we apply it to the pencil-beam irradiation dataset. The data are created by irradiating the center of each of the nine crystals with  $10^4$  monoenergetic  $\gamma$ -photons ( $E_\gamma = 511$  keV) being located 1 mm above the array's surface. For each recorded  $\gamma$ -interaction, the associated optical photon data are clustered and stored. Subsequently, the GAN is conditioned on the  $\gamma$ -photons interaction position inside the array, and the corresponding optical photon data are generated. Floodmaps are created by binning the COG positions computed for each recorded  $\gamma$ -photon. For the  $k$ th  $\gamma$ -photon producing  $N_k$  detected optical photons, the COG is calculated as the energy-weighted mean detection position,

$$\mathbf{R}_{\text{COG},k} = \frac{\sum_{i=1}^{N_k} E_i \mathbf{R}_i}{\sum_{i=1}^{N_k} E_i}, \quad (8)$$

where  $\mathbf{R}_i$  and  $E_i$  denote the detection position and energy of the  $i$ th optical photon, respectively.

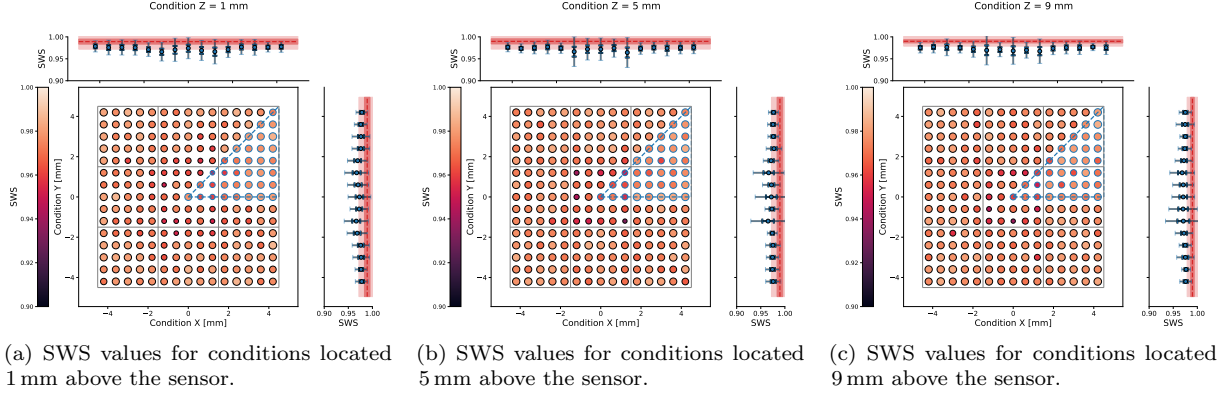


Figure 3: SWS results for the full array evaluation. The location of each scatter point represents the condition location, while the color visualizes the estimated SWS value. The row and column-wise results are depicted in the side and top plots. The blue point indicates the mean, and the bright and transparent error bars show one and three standard deviations. The dashed red line, with a bright and transparent red band, represents the baseline SWS performance (mean, one standard deviation, three standard deviations) achieved by two independent simulation runs with the same settings. Points with a blue edge color coincide with emission locations that were originally present during the training.

## 4. Results

### 4.1. Full Array Evaluation

The results of the full array evaluation are depicted in Figure 3. All SWS row and column values agree with the baseline Monte-Carlo simulation at least within a  $3\sigma$ -range (shown by the pink region around the red dashed line). Conditions outside the fundamental domain show the same similarity performance as conditions inside the fundamental domain. Furthermore, SWS values of conditions located in the lowest DOI-layer ( $Z = 1$  mm) and central crystal are slightly decreased compared to the values of the side and corner crystals. This effect is only partially observed for higher DOI-layers, where mostly only the conditions at the neighboring crystal boundaries show decreased values.

### 4.2. High-Resolution Evaluation

The results of the high-resolution evaluation are depicted in Figure 4. Considering the top and side plot, 85 % of the column and 100 % of the row SWS values agree with the Monte-Carlo ground truth within  $3\sigma$ . For a given DOI-layer, no systematic performance degradation is observed for evaluation conditions located further from training conditions (blue crosses). Points lying midway between training grid positions achieve comparable SWS values to those in immediate proximity of training data. The best performance is observed for lowest, middle and highest DOI-layer, while the layers in-between show a slightly decreased similarity. Similar to the previous evaluation, Section 4.1, SWS values of conditions located in the central crystal are lower than their counterparts within the side or edge crystal. Besides that, the plots reveal that conditions near the crystal boundary running parallel to the  $x$ -axis show better performance than conditions located along the crystal boundary parallel to the  $y$ -axis.

### 4.3. Pencil Beam Evaluation

The floodmap based on the GAN-generated optical photon data and Monte-Carlo simulation data is shown at Figure 5 with the estimated global SSIM value. Both SSIM values are within a  $3\sigma$ -agreement, with

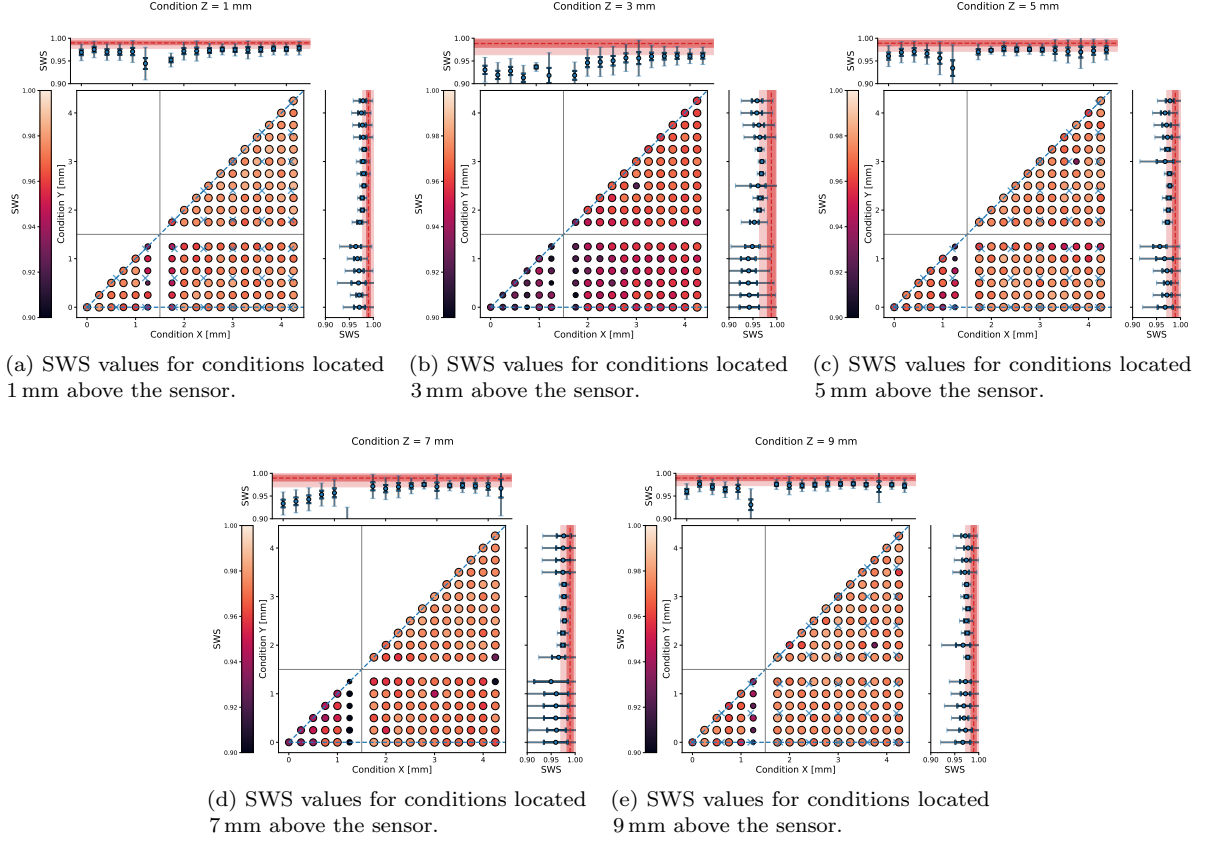


Figure 4: SWS results for the high-resolution evaluation. The location of each scatter point represents the condition location, while the color corresponds to the estimated SWS value. The row and column profiles are shown in the side and top plots. The blue point indicates the mean, and the bright and transparent error bars show one and three standard deviations. For conditions that are located in a row or column having fewer than four other conditions, the row or column-averaged standard deviation is used. The dashed red line, with a bright and transparent red band, represents the baseline SWS performance (mean, one standard deviation, three standard deviations) achieved by two independent simulation runs with the same settings. Transparent blue crosses ( $Z = 1\text{ mm}, 5\text{ mm}, 9\text{ mm}$ ) mark the emission locations that were originally present during training.

the baseline Monte-Carlo simulation achieving  $0.9799 \pm 0.0015$ , and  $0.9741 \pm 0.0018$ . The GAN is able to reproduce photopeak events as well as inter-crystal scatter events. Compared to the baseline Monte-Carlo simulation, the bright clusters at the array's corners show visually a bigger spread. A dominant artifact can be seen in the photopeak cluster of the central crystal, showing a cross-like structure.

The non-cumulative and cumulative distributions of the local SSIM values are displayed in logarithmic-scale in Figure 6a and Figure 6b. Both distributions show similarities in the distribution's peak region (local SSIM  $\geq 0.8$ ). Compared to the Monte-Carlo baseline whose distribution tail ends close to 0.193, the GAN's distribution has a longer tail towards lower SSIM values ending around -0.23. Figure 6c shows in red the regions where the local SSIM values of the GAN's COG distribution fall below the threshold of the baseline Monte-Carlo simulation. The image indicates that the lowest SSIM values (0.2 % of all local SSIM values) originate predominantly from the artifact region in the central crystal, with only minor contributions from the other photopeak clusters.

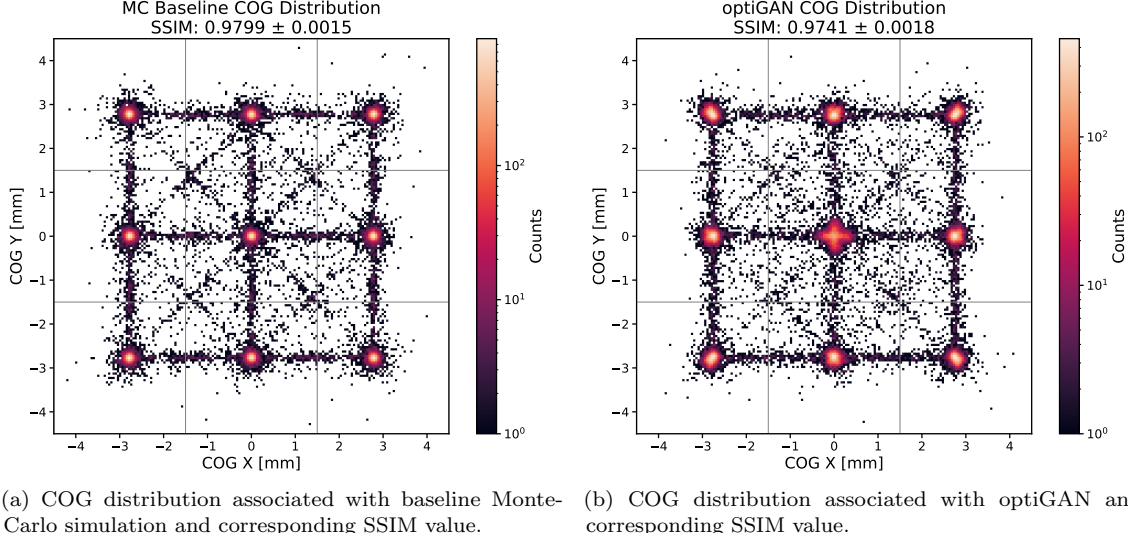


Figure 5: COG distribution generated by the baseline Monte-Carlo simulation and optiGAN (Left and right, respectively). Photopeak (bright clusters) and inter-scatter (lines) events are clearly visible in both figures. The gray grid represents the crystals of the detector array.

## 5. Discussion

The results of the full array evaluation demonstrate that the enhanced optiGAN model is able to generate optical photon data in good agreement with the ground truth simulation data. Since the similarity performance values between conditions located in the fundamental domain do not differ from conditions outside, the evaluation underlines the efficacy of our training approach. Although one could expect that the generation of high-fidelity data might be the easiest for conditions in the central region, results indicate that the similarity performance is decreased in that region compared to the side and corner crystals. One reason could be that the number of conditions, thus of training samples contained in the central crystal is the lowest at only  $\approx 17\%$  of all training data. Furthermore, there is a slight indication that the model works better for conditions located in a DOI-layer further away from the photosensor, pronounced through higher SWS values. This behavior can be explained by physics, since the spatial and momentum components conditioned for farther DOI layers show greater uniformity and symmetry.

The high-resolution experiment demonstrates the capabilities of the enhanced optiGAN model to generate high-fidelity optical photon data also for conditions never seen by the network. Results show that points near and far from training conditions achieve a similarity comparable to the ground truth. Similar to the full experiment, it is observed that the lowest similarity values are obtained for the central crystal, especially for conditions near the neighboring crystal. It can be expected that conditions near crystal boundaries are most challenging to model due to more complex light paths, reflection, and transmission characteristics. However, the same complex optical characteristics apply to crystal boundaries between side and corner crystals, yet the model shows higher similarity values than at the center. Therefore, we believe this issue arises from the asymmetry in the number of training conditions, considering crystal boundaries along the  $x$ -axis and  $y$ -axis. One possible solution to prevent this behavior could be switching to a fundamental domain of the  $D_2$  symmetry group, which equally includes horizontal and vertical crystal boundaries and covers a fourth of the array's cross-sectional area. In the current high-resolution experiment, conditions located at known (1 mm, 5 mm, 9 mm) and unknown (3 mm, 7 mm) crystal heights show no significant differences, while a slight but not statistically significant degradation was observed for decreasing height of the unknown DOI-layers.

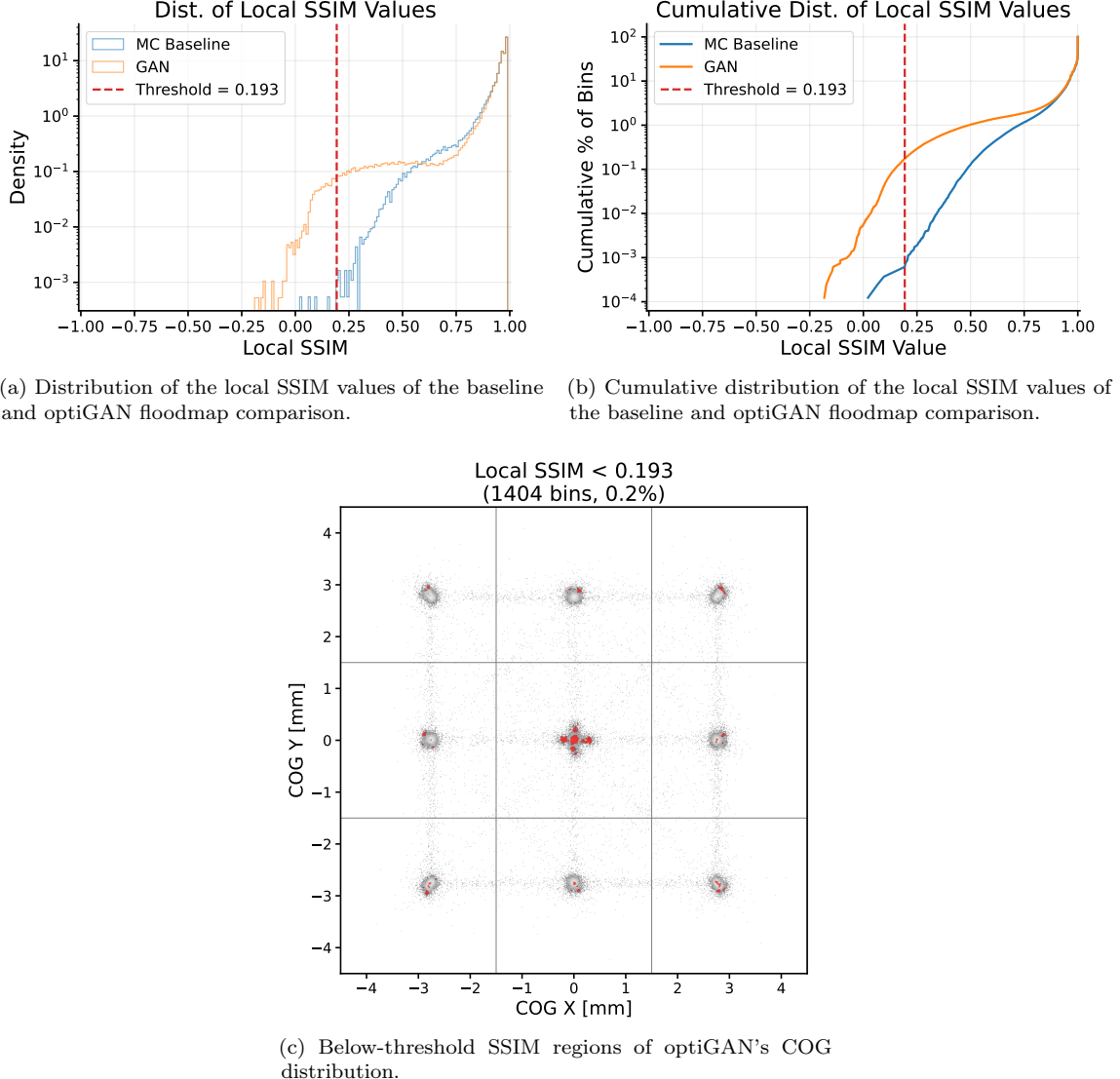


Figure 6: Local SSIM distributions of the baseline and optiGAN flood map comparison, and low SSIM regions. The set of local SSIM values is given by the SSIM estimate computed within a sliding window centered at each pixel location, capturing spatially resolved structural similarity across the image. The SSIM threshold was chosen to be equal to the lower end of the baseline simulation’s distribution tail.

The pencil beam evaluation analyzes the performance of the enhanced optiGAN model under common visual characteristics used in experimental radiation detector research. The global SSIM values of the optiGAN data and baseline Monte-Carlo simulation agree within  $3\sigma$ . The GAN is able to reproduce typical characteristics of COG-floodmaps like photopeak clusters and inter-crystal lines, which demonstrates the successful transition to realistic  $\gamma$ -photon data. Overall, one can notice that the cluster spots show a larger spread and at the corners and an asymmetric shape. Furthermore, the photopeak of the central crystal shows a cross artifact. Detailed analysis reveals that both foomaps have a similar peak progression of the local SSIM values, with a larger tail for optiGAN’s local SSIM values. Those larger values originate

mainly from the artifact of the central crystal, with minor contributions from the other photocluster regions. The cross artifact emerges from mispositioning of optical photons for the central crystal condition. Related to the aforementioned decreased similarity values of the central crystal, this observation supports our interpretation that the lower number of conditions at the center induces this issue. The non-circular photopeak cluster plots are likely due to machine learning-typical bias effects near data and condition limits. Since the overall structure shows very good agreement with the ground truth, and the optical photon data is typically forwarded to SiPM modeling, looking at a set of SPADs, we believe that those effects will not drastically change the result of the electronic modeling.

## 6. Summary & Outlook

In this work, we presented a novel optiGAN generation and demonstrated its ability to produce optical photon data within a  $3 \times 3$  BGO crystal array, using our recent LUT Davis model of optical crosstalk in pixelated detectors [30]. We enhanced optiGAN with Fourier components and a physics-informed loss function to model the complex light pattern of a crystal array, using the same generator and discriminator architectures as those used for a single-crystal optiGAN. We followed this approach to reduce computational burden and increase practicability, with consideration for users of the GEANT4 Application for Tomographic Emission (GATE) community.

The model demonstrated its ability to generate high-fidelity simulation data in good agreement with ground-truth Monte Carlo simulations. Furthermore, the model demonstrated strong generalization and interpolation capabilities across conditions (emission points) not present during training. Minor asymmetrical similarity differences between row and column evaluations of the high-resolution grid indicate that the fundamental training domain, covering an eighth of the array's cross-section, may need to be extended to a quarter of the cross-sectional area. Evaluating the generated data using standard experimental metrics showed very good agreement with the ground-truth simulation.

In the future, we will optimize hyperparameters of the enhanced optiGAN model to improve its performance. Our current architecture prioritizes accessibility for the GATE user community, which may lack access to high-performance computing resources. However, we expect that combining our architectural improvements with deeper networks will yield further performance gains for users with more powerful hardware. Furthermore, we will demonstrate that the model can be used to create specific physics scenarios, e.g., condition inter-crystal scattering to occur in selected regions, which is difficult to achieve in classical Monte-Carlo simulations. Ultimately, we aim at developing an optiGAN model that generalizes across different array configurations.

## 7. Acknowledgment

This work is supported by NIBIB grant R01 EB034475.

## References

- [1] Michael E. Phelps et al. "Application of Annihilation Coincidence Detection to Transaxial Reconstruction Tomography." In: *Journal of Nuclear Medicine* 16.3 (Mar. 1975). Publisher: Society of Nuclear Medicine Section: Article, pp. 210–224.
- [2] Dale L Bailey et al., eds. *Positron Emission Tomography: Basic Sciences*. London: Springer, 2005. doi: 10.1007/b136169.
- [3] Simon R. Cherry, James A. Sorenson, and Michael E. Phelps. *Physics in Nuclear Medicine*. 4th ed. 2012.
- [4] Eric Berg and Simon R. Cherry. "Innovations in Instrumentation for Positron Emission Tomography." In: *Seminars in Nuclear Medicine: Instrumentation* 48.4 (July 2018), pp. 311–331. doi: 10.1053/j.semnuclmed.2018.02.006.
- [5] David Sarrut et al. "Advanced Monte Carlo simulations of emission tomography imaging systems with GATE." en. In: *Physics in Medicine & Biology* 66.10 (May 2021). Publisher: IOP Publishing, 10TR03. doi: 10.1088/1361-6560/abf276.
- [6] David Sarrut et al. "GATE 10 Monte Carlo particle transport simulation -Part I: development and new features." In: *Physics in Medicine & Biology* (2025). doi: 10.1088/1361-6560/ae237b.
- [7] Nils Krah et al. "GATE 10 Monte Carlo particle transport simulation -Part II: architecture and innovations." en. In: *Physics in Medicine & Biology* (2025). doi: 10.1088/1361-6560/ae237c.
- [8] Luke de Oliveira, Michela Paganini, and Benjamin Nachman. "Learning Particle Physics by Example: Location-Aware Generative Adversarial Networks for Physics Synthesis." en. In: *Computing and Software for Big Science* 1.1 (Sept. 2017), p. 4. doi: 10.1007/s41781-017-0004-6.
- [9] Michela Paganini, Luke de Oliveira, and Benjamin Nachman. "Accelerating Science with Generative Adversarial Networks: An Application to 3D Particle Showers in Multilayer Calorimeters." en. In: *Physical Review Letters* 120.4 (Jan. 2018), p. 042003. doi: 10.1103/PhysRevLett.120.042003.
- [10] Michela Paganini, Luke de Oliveira, and Benjamin Nachman. "CaloGAN: Simulating 3D high energy particle showers in multilayer electromagnetic calorimeters with generative adversarial networks." en. In: *Physical Review D* 97.1 (Jan. 2018), p. 014021. doi: 10.1103/PhysRevD.97.014021.
- [11] D. Sarrut, N. Krah, and J. M. Létang. "Generative adversarial networks (GAN) for compact beam source modelling in Monte Carlo simulations." en. In: *Physics in Medicine & Biology* 64.21 (Oct. 2019). Publisher: IOP Publishing, p. 215004. doi: 10.1088/1361-6560/ab3fc1.
- [12] C. Fanelli. "Machine learning for imaging Cherenkov detectors." en. In: *Journal of Instrumentation* 15.02 (Feb. 2020), pp. C02012–C02012. doi: 10.1088/1748-0221/15/02/C02012.
- [13] Cristiano Fanelli and Jary Pomponi. "DeepRICH: Learning Deeply Cherenkov Detectors." In: *Machine Learning: Science and Technology* 1.1 (Apr. 2020). arXiv:1911.11717 [hep-ex, physics:nucl-ex, physics:physics], p. 015010. doi: 10.1088/2632-2153/ab845a.
- [14] D Sarrut et al. "Modeling complex particles phase space with GAN for Monte Carlo SPECT simulations: a proof of concept." en. In: *Physics in Medicine & Biology* 66.5 (Mar. 2021), p. 055014. doi: 10.1088/1361-6560/abde9a.
- [15] Carlotta Trigila, Anirudh Srikanth, and Emilie Roncali. "A generative adversarial network to speed up optical Monte Carlo simulations." en. In: *Machine Learning: Science and Technology* 4.2 (June 2023), p. 025005. doi: 10.1088/2632-2153/acc782.
- [16] Carlotta Trigila et al. "Towards large nuclear imaging system optical simulations with optiGAN, a generative adversarial network." en. In: *Physics in Medicine & Biology* 70.12 (June 2025). Publisher: IOP Publishing, p. 125002. doi: 10.1088/1361-6560/adde0c.
- [17] Guneet Mummaneni et al. "optiGAN: a deep learning-based alternative to optical photon tracking in Python-based GATE (10+)." en. In: *Physics in Medicine & Biology* 70.13 (July 2025). Publisher: IOP Publishing, p. 135009. doi: 10.1088/1361-6560/ade2b5.
- [18] Ian J. Goodfellow et al. *Generative Adversarial Networks*. en. arXiv:1406.2661 [stat]. June 2014. doi: 10.48550/arXiv.1406.2661.
- [19] Mehdi Mirza and Simon Osindero. *Conditional Generative Adversarial Nets*. en. arXiv:1411.1784 [cs]. Nov. 2014. doi: 10.48550/arXiv.1411.1784.
- [20] Martin Arjovsky, Soumith Chintala, and Léon Bottou. *Wasserstein GAN*. en. arXiv:1701.07875 [stat]. Dec. 2017. doi: 10.48550/arXiv.1701.07875.
- [21] Ali Rahimi and Benjamin Recht. "Random Features for Large-Scale Kernel Machines." In: *Advances in Neural Information Processing Systems*. Vol. 20. Curran Associates, Inc., 2007.
- [22] Matthew Tancik et al. "Fourier Features Let Networks Learn High Frequency Functions in Low Dimensional Domains." In: *Advances in Neural Information Processing Systems*. Vol. 33. Curran Associates, Inc., 2020, pp. 7537–7547.
- [23] Tero Karras, Samuli Laine, and Timo Aila. "A Style-Based Generator Architecture for Generative Adversarial Networks." en. In: () .
- [24] Ishaan Gulrajani et al. *Improved Training of Wasserstein GANs*. arXiv:1704.00028 [cs]. Dec. 2017. doi: 10.48550/arXiv.1704.00028.
- [25] Emilie Roncali and Simon R Cherry. "Simulation of light transport in scintillators based on 3D characterization of crystal surfaces." en. In: *Physics in Medicine & Biology* 58.7 (Mar. 2013). Publisher: IOP Publishing, p. 2185. doi: 10.1088/0031-9155/58/7/2185.
- [26] Emilie Roncali et al. "Cerenkov light transport in scintillation crystals explained: realistic simulation with GATE." en. In: *Biomedical Physics & Engineering Express* 5.3 (Apr. 2019). Publisher: IOP Publishing, p. 035033. doi: 10.1088/2057-1976/ab0f93.
- [27] Carlotta Trigila and Emilie Roncali. "Integration of polarization in the LUTDavis model for optical Monte Carlo simulation in radiation detectors." en. In: *Physics in Medicine & Biology* 66.21 (Oct. 2021). Publisher: IOP Publishing, 21NT03. doi: 10.1088/1361-6560/ac2e18.
- [28] Zhou Wang et al. "Image quality assessment: from error visibility to structural similarity." In: *IEEE Transactions on Image Processing* 13.4 (Apr. 2004), pp. 600–612. doi: 10.1109/TIP.2003.819861.

- [29] Danilo Bronzi et al. “SPAD Figures of Merit for Photon-Counting, Photon-Timing, and Imaging Applications: A Review.” In: *IEEE Sensors Journal* 16.1 (Jan. 2016), pp. 3–12. doi: [10.1109/JSEN.2015.2483565](https://doi.org/10.1109/JSEN.2015.2483565).
- [30] Carlotta Trigila et al. “Intercrystal Optical Crosstalk in Radiation Detectors: Monte Carlo Modeling and Experimental Validation.” In: *IEEE Transactions on Radiation and Plasma Medical Sciences* 8.7 (Sept. 2024), pp. 734–742. doi: [10.1109/TRPMS.2024.3395131](https://doi.org/10.1109/TRPMS.2024.3395131).